

# A HYBRID ALGORITHM FOR PERIOD ANALYSIS FROM MULTI-BAND DATA WITH SPARSE AND IRREGULAR SAMPLING FOR ARBITRARY LIGHT CURVE SHAPES

ABHIJIT SAHA

National Optical Astronomy Observatories, 950 N. Cherry Ave, Tucson, AZ 85719

A. KATHERINA VIVAS

Cerro Tololo Inter-American Observatory, National Optical Astronomy Observatories, Casilla 603, La Serena, Chile

## ABSTRACT

Ongoing and future surveys with repeat imaging in multiple bands are producing (or will produce) time-spaced measurements of brightness, resulting in the identification of large numbers of variable sources in the sky. A large fraction of these are periodic variables: compilations of these are of scientific interest for a variety of purposes. Unavoidably, the data-sets from many such surveys not only have sparse sampling, but also have embedded frequencies in the observing cadence that beat against the natural periodicities of any object under investigation. Such limitations can make period determination ambiguous and uncertain. For multi-band data sets with asynchronous measurements in multiple pass-bands, we want to maximally utilize the information on periodicity in a manner that is agnostic of differences in the light curve shapes across the different channels. Given large volumes of data, computational efficiency is also at a premium. This paper develops and presents a computationally economic method for determining periodicity which combines the results from two different classes of period determination algorithms. The underlying principles are illustrated through examples. The effectiveness of this approach for combining asynchronously sampled measurements in multiple observables that share an underlying fundamental frequency is also demonstrated.

*Keywords:* methods: data analysis, stars: variables

## 1. INTRODUCTION

A common problem in time-domain astronomy is the identification and determination of periodicity in variable phenomena. The available data are all too often sparsely sampled, with irregular intervals taken with cadences which themselves have embedded periodicities that beat against any periodicity and harmonics present in the variable phenomena being investigated. In the face of this, astronomers have historically been quite resourceful at coaxing out periodicities from data that are beset with aliasing and noise. A comprehensive review of the various techniques (which have grown in complexity as computational power has increased) falls outside the scope of this paper. The reader can find an admirable recent review in Graham et al. (2013). The deluge of variability data from future surveys such as the Large Synoptic Survey Telescope (LSST) will have irregular and sparse sampling, measurements in multiple passbands that are separated in time from band to band, and embedded periodicities in the cadence (diurnal, lunar and annual cycles as well as from chosen cadences). This paper presents a procedure that seeks to combine the most computationally fast existing procedures to produce a robust technique for period determination in the face of such sub-optimal data.

The last decade has produced several time-domain photometric surveys, e.g. the Catalina Real-Time Transient Survey (Drake et al. 2009), the Palomar Transient Factory (Law et al. 2009; Rau et al. 2009), Pan-STARRS (Chambers et al. 2016), and Kepler (Koch et al. 2010) to name a few, which have added to the legacy of MACHO (Alcock et al. 1992, 1996), OGLE (Udalski et al. 1993) and ASAS (Pojmanski 2002). All of these are slated to be dwarfed by the 10 year projected survey with Large Synoptic Survey Telescope (LSST) which is currently under construction. While many of the above named projects were exclusively time-domain surveys, the broader mission of the LSST survey will result in collecting brightness measures for a given source in the sky at  $\sim 1000$  epochs spread over 10 years. These  $\sim 1000$  visits will be spread over 6 different passbands, so that there will be between 100 to 200 total samples in any

given passband. Thus at the end of the first year’s observing season, we can expect there to be between 10 to 20 epochs for a given object on average in any given passband. The observations in different bands will not be near simultaneous, so in principle there will be up to 100 epochs in total spread over all passbands. Even though we can expect that the observing cadence might ensure that each part of the sky gets visited oftener than the average cadence at some times over the 10 year survey, early determination of light curves will surely be at a premium for any and all variable sources. An efficacious method for gleaning periodicities early in the survey from such sparse sampling over varied passbands is thus desirable.

The authors of this paper have recently been engaged in a time-domain survey of the Galactic bulge area with the DECam imager ([Flaugher et al. 2015](#)) on the 4-m Blanco telescope at CTIO. Observations have been made of 6 select fields, in 5 different passbands. Although the cadence was optimized for characterizing RR Lyrae stars (the primary purpose of the survey), the sampling remains sparse, and with embedded periodicities in the sampling pattern (diurnal, lunar, and annual cycles). Also, given the multiple passbands, the data-set provides a good test bed for examining how partial information from the individual bands can be combined to infer periodicity information that is common to all. The methodology presented in this paper was developed to improve the efficiency of period determination and identification of desired variable stars from over 20,000 objects flagged as variable.

Existing methods for period determination can be broadly binned into two classes. In the first, the data are folded by a set of trial periods, so that each observation at time  $t$  with measured magnitude  $m$  can be assigned a phase  $\phi$ . We then look for order in this  $(\phi, m)$  plane, such that at the correct  $P$ , the observations fall along a narrow locus that spans the range of  $\phi$ . No prior assumption need be made of the light curve shape, and the approach is shape agnostic. Differences between methods of this ilk, which we label as the ‘Phase Folding Method’ (PFM), lie in how they go about measuring the scatter of the observations in the  $(\phi, m)$  plane. The second class of methods uses harmonic analysis (HA): Fourier and wavelet based methods fall into this category. A specific implementation is to invoke the properties of the Fourier series where the orthonormality of Fourier coefficients for a harmonic progression of putative periods can be used to uniquely describe any periodic signal of any shape. There are two notable issues: 1) deriving the Fourier spectrum requires regular sampling, which hardly any astronomical data-sets provide, so a proxy for the Fourier spectrum is often used; and 2) the shape of the light curve is manifest in the Fourier power-spectrum as the relative strength and phases at different frequencies. We do not consider template fitting methods here: while they are very useful if you know the shape of the light curve, our interest is in the more general case where the shape is unconstrained. In this paper a representative method from each of the PFM and harmonic analysis classes has been chosen. The selection favored algorithms that are computationally straightforward and economical, and which, in the authors experience, have been gainfully employed across a variety of period searching projects over the past several decades, thus authenticating their robustness. While within each class one particular implementation may better another marginally, this paper shows that substantive gains are to be had by combining results across the two classes since they provide complementary information on the true period.

In section § 2, we show how these methods respond to different kinds of variable signals, with differing sampling density, cadence, and noise. A new period discriminator (that combines information from the PFM and harmonic analysis classes) is introduced, and its efficacy is demonstrated. The two chosen methods from each of the classes mentioned above are described and applied to archetypal examples spanning different shapes of light curves, different sampling patterns, sparseness, and noise, gradually increasing in complexity. The pedagogical walk through the examples illuminates the strengths and weaknesses of the two classes of methods. A statistic that combines the analysis from both classes is introduced, and its efficacy is illustrated through the examples considered. In § 3, key constraints that govern how densely spaced the search for periods or frequencies must be are discussed. In § 4 a real multi-band data-set for an RR Lyrae star is examined, and it is shown how the new discriminant for the individual bands can be combined to reinforce information across bands. § 5 discusses how confidence estimates are generated for the new discriminant. § 6 applies the methodology for an observational cadence simulated for LSST, to show that it works for asynchronous measurements made in the different pass-bands. Computer code in the IDL language is provided via *github*, as described in the Appendix. The problem of combining asynchronous measurements from different channels (e.g. multiple passbands) to derive the underlying common fundamental period has also been addressed by [VanderPlas & Ivezić \(2015\)](#) and by [Mondrik et al. \(2015\)](#), both wholly within the HA approach. We comment on how the method presented in this paper differs from theirs in the concluding discussion in § 7

## 2. PERIOD ANALYSIS FROM A SINGLE OBSERVABLE

It is useful first to assign specific meaning to terms that are used in this paper. The term ‘time-sequence’ will refer to the data-set being analyzed, i.e. a set of data-points with observation time  $t$ , and the time dependent variable, such as

flux, magnitude, velocity, etc, is designated by  $m$ . We are interested here in periodic behavior: when a time-sequence is folded by a period  $P$  (whether assumed or real), it produces a ‘light curve’ where the data-points  $m$  are assigned a phase  $\phi$ .

$$\phi = t/P \text{ modulo } 1 \quad (1)$$

We use the term ‘periodogram’ for the period/frequency spectrum of *any* periodicity indicating metric. For a given astrophysical object, we may have more than one observed quantity that is varying in time, e.g. magnitude and velocity, or magnitudes in different passbands. These share a common periodicity, although they may have quite different wave-forms in these different apparitions. Said another way, all of these quantities share a *fundamental period*, but differ in the relative strengths of the higher harmonics. We address here the problem of how best to find the fundamental period, and in the methodology of combining information from multiple observed quantities that share it.

### 2.1. The Phase Folding Method: Phase Dispersion Minimization and the Lafler-Kinman approach

The phase dispersion minimization (PDM, [Stellingwerf 1978](#)) method is based on the idea that if the time-sequence data are folded by the correct period  $P$ , the resulting light curve shows minimal scatter within all bins in phase. The sum of the scatter (or net dispersion) from all bins is obtained for each trial period, and the period for which this sum is the smallest is notionally the correct period. The binning need not be done to keep equal bin sizes: for sparse data, where phase coverage (which changes with assumed period) is likely to be uneven, it is possible to use an adaptive binning strategy using all possible bins, each with  $n$  points. A widely used implementation of this technique which precedes the [Stellingwerf \(1978\)](#) generalized PDM method, is the Lafler-Kinman (LK, [Lafler & Kinman 1965](#)) procedure, which is in effect a special case of PDM, with adaptive binning and  $n = 2$ . The choice of minimal  $n$  is particularly suitable for sparse data, since it keeps the bins as narrow as the data will allow. It is chosen here as the representative of the PFM class because it is computationally the most economical, conceptually the simplest, and has served the senior author of this paper well for over three decades.

The Lafler-Kinman statistic  $\Theta$  at a given period  $P$  is given by:

$$\Theta = \frac{\sum_{i=1}^N (m_i - m_{i-1})^2}{\sum_{i=1}^N (m_i - \bar{m})^2} \quad (2)$$

where the  $N$  measurements  $m_j$  at times  $t_j$  have been folded with period  $P$  to produce phases  $\phi_j$  in accordance with eqn. 1 and sorted in ascending order of  $\phi$ , to get ordered pairs  $(\phi_i, m_i)$ . In addition, in the phase sorted arrays,  $(\phi_0, m_0)$  is set equal to  $(\phi_N, m_N)$ , which completes the phase cycle.  $\bar{m}$  is the mean of all  $m_i$ . This formula assumes equal weighting of all points. Let

$$w_i = \frac{1}{(\sigma_i^2 + \sigma_{i-1}^2)} \quad (3)$$

where  $\sigma_i$  is the uncertainty in  $m_i$ . The Lafler-Kinman can then be modified as:

$$\Theta = \frac{\sum_{i=1}^N w_i (m_i - m_{i-1})^2}{\sum_{i=1}^N (m_i - \bar{m})^2 \cdot \sum_{i=1}^N w_i} \quad (4)$$

where  $\bar{m}$  is correspondingly the weighted mean over  $m_i$ .

As for any PFM class method, a strength of the LK approach is that it makes no assumption about the shape of the light curve. A weakness is that as data get sparse, the gaps in successive phase in the folded trial light curves can become very different from one period to another, resulting in periodograms (period vs. net dispersion) with increasing false structure which can interfere with the identification of the true period. Thus in addition to aliasing, there are spurious minima produced in the periodogram that are introduced by the paucity of data. For practical applications, it is important to consider limitations on the step-size between successive trial periods, so that the true period is not missed: details are discussed later in § 3.

### 2.2. Harmonic Analysis and the Lomb-Scargle approach

Any periodic function with arbitrary shape that is piece-wise continuous with a finite number of finite discontinuities (Dirichlet’s conditions) can be represented by a Fourier series with frequencies that are integer multiples of the fundamental frequency. Thus period analysis of evenly spaced time-series data is straightforward. For uneven spacing, to perform a strict Fourier analysis, the data must be re-sampled evenly. The re-sampling process can be computationally

expensive, and can introduce significant spurious structure in the Fourier power spectrum. Alternatively, the amplitude of a fitted sine(/cosine)-wave at a given frequency can be used to glean the Fourier power at that frequency, and a periodogram can thus be constructed over desired frequencies, thereby eliminating the need to re-sample the data. Credit for implementing the latter approach to astronomy applications belong to [Lomb \(1976\)](#) and [Scargle \(1982\)](#). The eponymous Lomb-Scargle algorithm is available in various coding languages.

A Fourier transform (FT) or a Lomb-Scargle (LS) periodogram<sup>1</sup> contains information not only of the fundamental period, but also of the waveform shape, which appear as sub-dominant peaks in the periodogram. With well and plentifully sampled data, this can be an advantage, but this additional signal can ironically also be a source of confusion when the data are sparse and sampled with embedded periodicities that produce aliasing. If the signal being sampled is a pure sine wave, ideal sampling in the absence of noise will produce a single peak in the periodogram. However, missing data has the effect of redistributing power into alias frequencies (and phases): essentially a convolution of the true frequency peak with a frequency dependent function that represents the actual sampling (often called the ‘window function’). To see this, consider a signal  $U(t')$  (true time-series), which is measured at discrete times  $\tau_k$ . The available data can be re-sampled into an even time series  $S(t_i)$ , where

$$S(t_i) = U(t_i) \cdot W(t_i) \quad (5)$$

where  $W(t_i) = 1$  when the time bin  $t_i$  contains any of  $\tau_k$ , and 0 otherwise. The Fourier domain manifestation of the sampled signal  $S$  is then the convolution of the Fourier domain representations of the ‘true’ signal  $U$  and the ‘window function’  $W$ .

For non-sinusoidal variation, the Fourier coefficients representing higher harmonics are also convolved by the window-function, potentially creating confusion. Noise is an additional complication, since a full harmonic analysis will also seek to fit individual excursions due to noise, generating a Fourier spectrum that has power at frequencies other than the fundamental frequency or its harmonics. Thus a periodogram in general contains components other than those from the source due to noise and missing data.

In the following subsections we examine a set of simple examples of how the LK and the LS methods react to different waveforms, both in the well sampled and sparsely sampled instances, as well as when there is periodicity in the sampling windows. The examples illustrate the ideas mentioned above. We also see how the differences in how these methods respond can be used to our advantage: that the simultaneous application of both methods can be used to mitigate confusion that each of them generates singly. An ensuing hybrid statistic that reinforces information about the fundamental period/frequency from independent sampling of multiple quantities is developed and demonstrated for real world data.

### 2.3. Comparison of Lomb-Scargle and Lafler-Kinman methods in different situations

A few elementary examples best help to contrast and compare the relative strengths and weaknesses of the two methods. First consider a sine wave signal with a period  $P_0$  of 40 units, sampled over a total duration of 1000 units. The data are sampled at random instances with mean spacing of one unit, totaling 1000 samples. The top panel of Fig. 1 shows the resulting LS power ( $\Pi$ ) spectrum, with a strong peak at the 40 unit period of the signal. The LS analysis was done using a harmonic series in period (arithmetic series in frequency) so that the Fourier coefficients at each sampled frequency are mutually orthogonal (more on the details of choosing intervals are in § 3). The next panel shows what happens when only 5% of the original data, picked at random, are used. The resulting periodogram has power from the 40 unit peak re-distributed (random periodicities present in the sampling window due to the drastic reduction in sampling). The third panel shows the inverse (actually  $2/\Theta$ , since for random un-periodic variation  $\Theta$  tends to 2) of the Lafler -Kinman statistic  $\Theta$  of the full data set described here - so instead of the traditional minima in  $\Theta$ , we look for peaks in  $2/\Theta$  to be commensurate with  $\Pi$  from the LS algorithm. It does not do quite as well, because in addition to the expected peak in  $2/\Theta$  at 40 units, there are additional peaks at sub-harmonic frequencies, i.e. at integer multiples of the true period. This is because at these frequencies the ‘light curve’ simply repeats multiple times within the time-span of the putative period, and the LK statistic  $\Theta$  returns favorable values for those putative periods. The fourth panel is again the LK periodogram, but when only 5% of the data are used. For a pure sine-wave, clearly the FFT approach is the one that better isolates the true period. The final panel shows a hybrid quantity  $\Psi$  for the sub-sampled data, where  $\Psi$  is defined as:

$$\Psi = 2\Pi/\Theta \quad (6)$$

<sup>1</sup> the LS periodogram is considered henceforth as having the same properties of an FT, which it does if the frequencies sampled are part of a harmonic series

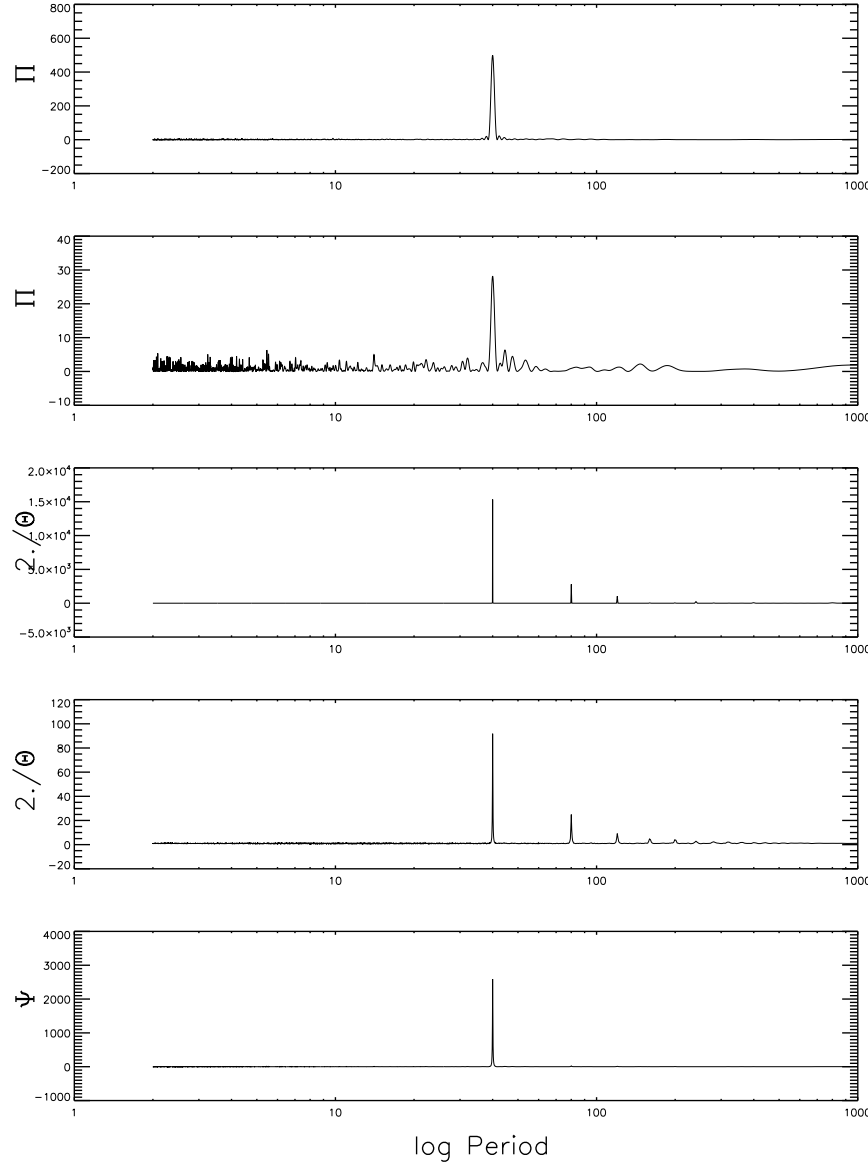


**Figure 1.** Top panel shows the Lomb-Scargle (LS) power spectrum (plotted vs. log period) for a repeating sine wave with period of 40 units. The data are sampled 1000 times randomly, but distributed uniformly, over a duration of 1000 units. A single strong peak at 40 units is seen as expected. The second panel shows what happens when only 5% of the original samples (picked at random) are used. The third panel shows the reciprocal of the Lafler-Kinman (LK) statistic  $\Theta$  for the same data: which produces sub-harmonic features. The fourth panel shows the  $\Theta$  statistic for the same 5% sub-sample of the data. The bottom panel shows the combined statistic  $\Psi$  for the sparsely sampled data. See § 2.3 for details and explanation.

Notice how the  $\Psi$  spectrum shows the true period with better definition than either  $\Pi$  or  $\Theta$  in panels two and four, and the sub-harmonics seen in  $\Theta$  are completely suppressed. We will see in the next examples that this is an even more useful metric in more complicated situations.

Next consider the case of an eclipsing light curve, which is flat over a 0.8 range in phase, with an eclipse modeled in the 0.2 interval of phase as a symmetrical triangular fall and rise. The period is again 40 units. It is sampled at random a 1000 times over a 1000 unit baseline. The observations times and signal strength are shown in the top panel of Fig. 2, which when folded by the correct period (40 units), yields the light curve in the second panel. The third

panel shows the situation when only 5% of the sample points are available, and the last panel shows the corresponding measurements when phased with the correct period.

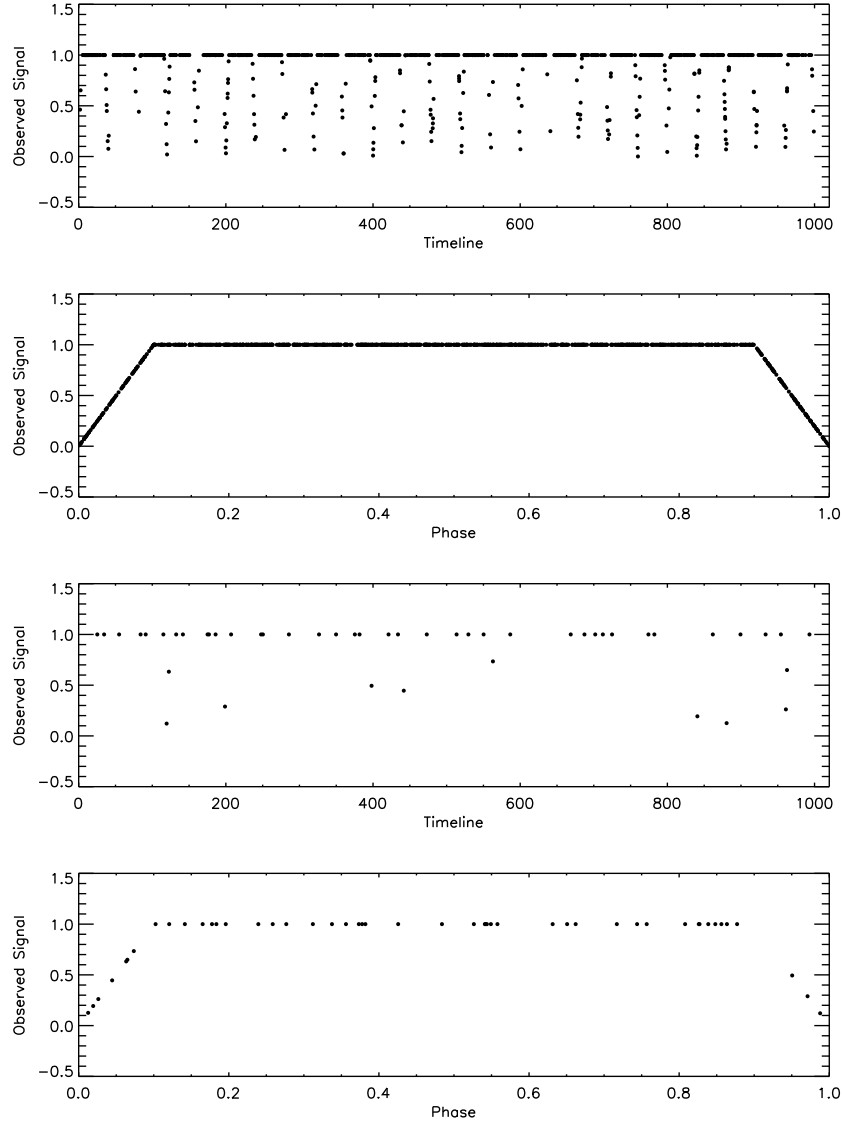


**Figure 2.** This figure visualizes the the observation times, phases and observed values from model eclipsing source described in § 2.3. The top panel shows the observation epochs and observed signal, which when folded by the correct period, yields the phased light curve in the second panel, which corresponds to the model described. In the third panel we see what happens when only 5% of the observations (chosen at random) are available, with the the fourth panel showing the resulting phased light curve, now relatively sparsely sampled.

Fig. 3 shows the periodograms for these cases. Notice that in the top panel, the higher harmonic frequencies that decompose the shape are clearly visible as peaks at shorter periods. In the second panel, where only 5% of the sample points are available, there is added confusion, as the secondary peaks become poorly resolved. The third panel, for the LK analysis of the exact same data, shows the harmonics very weakly if at all, since the LK method is shape agnostic. As in the previous case, the LK periodogram continues to show power at sub-harmonic frequencies. The second and fourth panels show the same analyses, but for only 5% of the sample points taken at random: the periodograms are

similar, but with added noise-like confusion. Note that in the final panel,  $\Psi$ , which combines results in the second and fourth panels, recovers the fundamental period with the least confusion. The LK and LS periodograms appear to each subdue the specious features of the other.

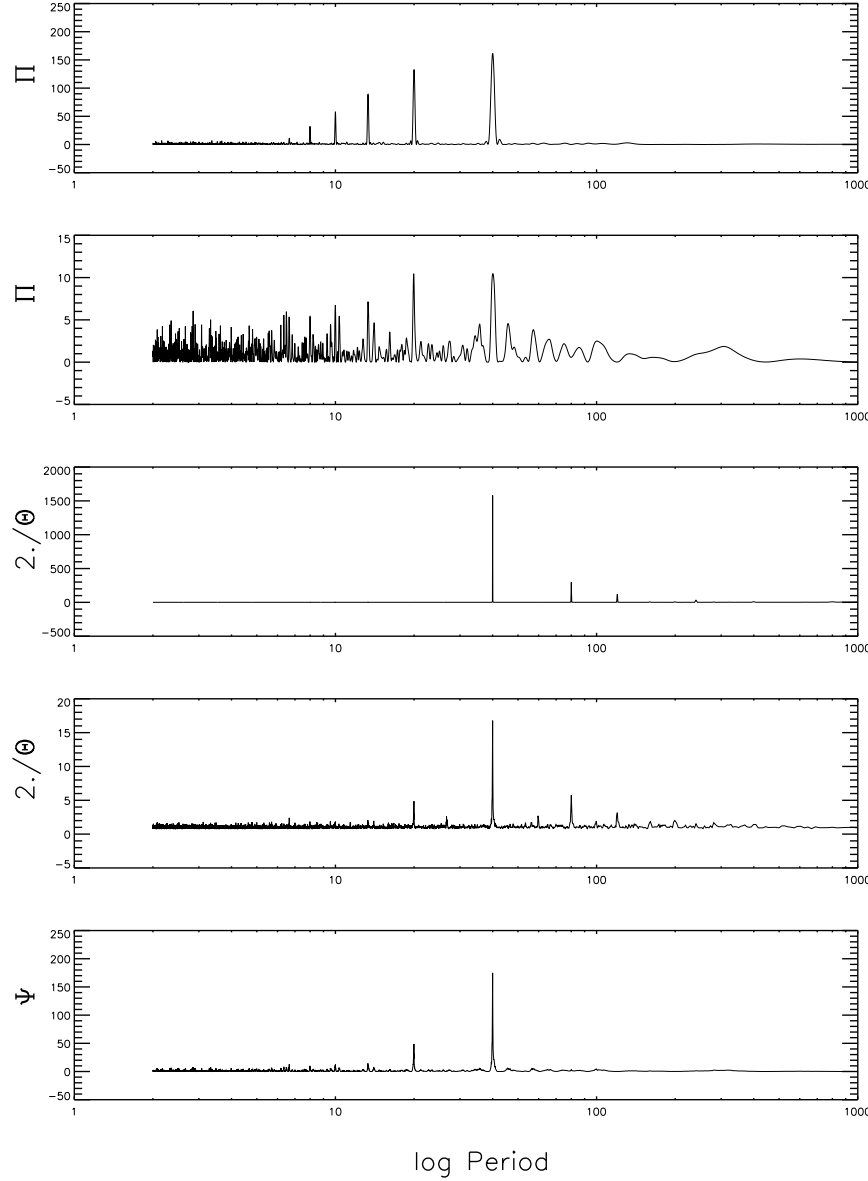


**Figure 3.** Here shown are the results for a model light curve with an eclipse described in § 2.3 and illustrated in Fig 2. The top panel is the LS power spectrum for a 1000 samples taken at random times, but with uniform distribution across the 1000 unit time baseline. The second panel is the same but with only 5% of the sample points drawn at random. The third and fourth panel are for time samples identical to that for panels one and two respectively, but showing the inverse of the LK statistic as in Fig. 1. The bottom panel shows the combined statistic  $\Psi$  for the sparsely sampled data. Note the power at harmonic frequencies in the Fourier spectrum that are absent in the LK spectrum. See § 2.3 for details and explanation.

Now we look at the effect of periodicities present in the sampling of the data: consider the same eclipsing light curve with the 40 unit period, which is again sampled at random, but with repetitive sampling windows with period 100 units. During each such 100 unit period, samples can be taken only during the first 30 units (analogous to the duration

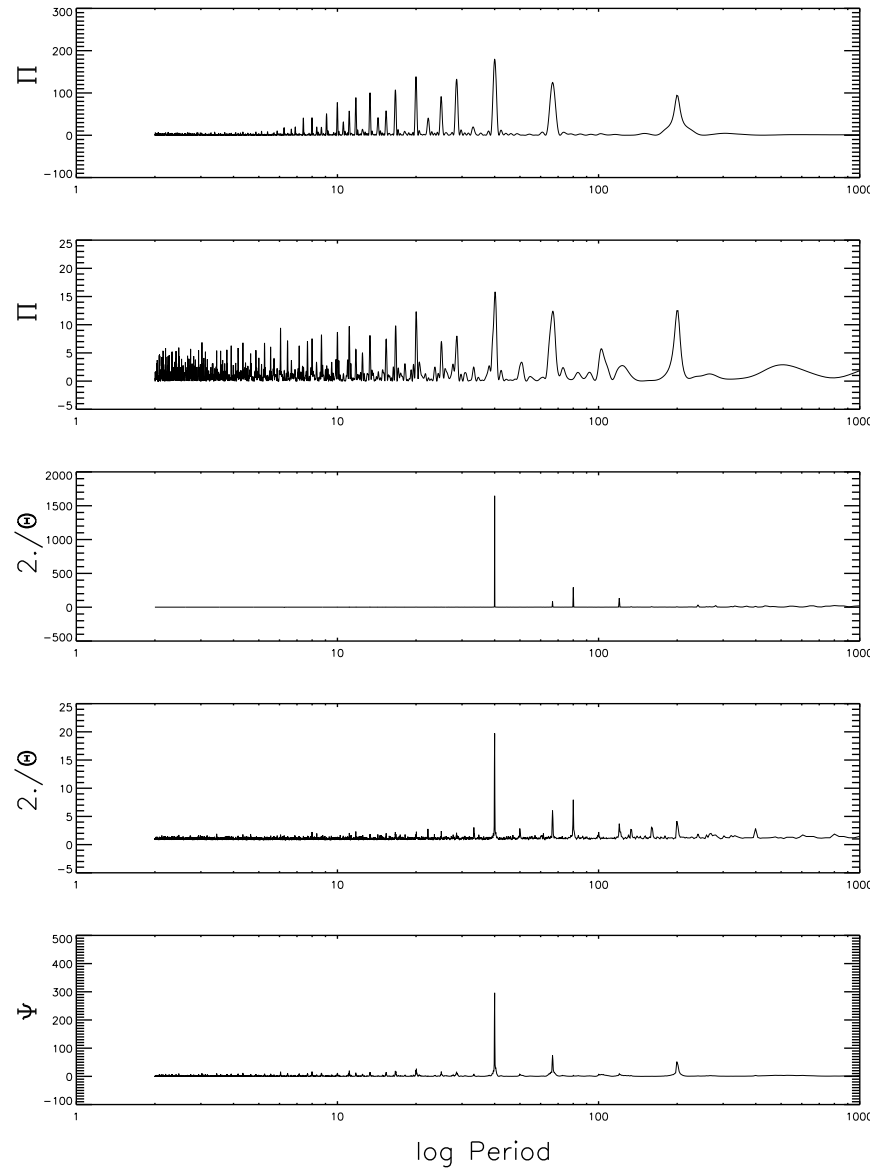


**Figure 4.** This case differs from that in Fig. 3 in only one way, in that the samples are taken according to a repeating pattern: sampling is allowed for a duration of 30 units, followed by a disallowed duration of 70 units. This 100 unit sampling-window cycle repeats periodically. Samples are taken at random times during the allowed intervals. In panels one and three, a total of 1000 samples are used, while in panels two and four, only 5% of the sampled data are used. Notice how the beating of the sampling window adds peaks to the LS power spectrum *as well as* to the LK  $\Theta$  spectrum.

of a night). This periodic sampling pattern beats against the periodicity in the signal, and the results are shown in Fig. 4. Note how additional prominent peaks have appeared at the beat frequencies  $P_b$ , where

$$1/P_b = 1/P \pm 1/P_w \quad (7)$$

where  $P_w$  is the periodicity of the sampling window (in this case 100 units), and  $P$  represents not only the fundamental period of the source, but also its harmonics. This results in a ‘forest’ of specious peaks. Real sampling in astronomy is often infused not only with diurnal observing windows, but also with lunation and annual cycles, often resulting in a forest of such beat peaks. The LK spectrum also sees the satellite alias periods with respect to the fundamental period, but being less sensitive to intrinsic harmonics (or shape of the light curve) is less affected at periods shorter

than the true fundamental period. We also see specious peaks on the sub-harmonic side, since the convolving function due to embedded frequencies in the sampling window has lobes on both sides. The  $\Psi$  spectrum reflects the best of both the LS and LK algorithms, and is the least confused.

In the final example, we add noise to the above case. To each sampled value, we add a random excursion drawn from a normal distribution with  $\sigma = 0.20$ , where the amplitude of the varying signal is unity. The net observational situation is illustrated in Fig. 5: the top panel shows the actual observation times and values, and the second panel shows the light curve when the observations are phased with the correct period. The third and fourth panels show the situation when a subset only 5% of the measurements are available.

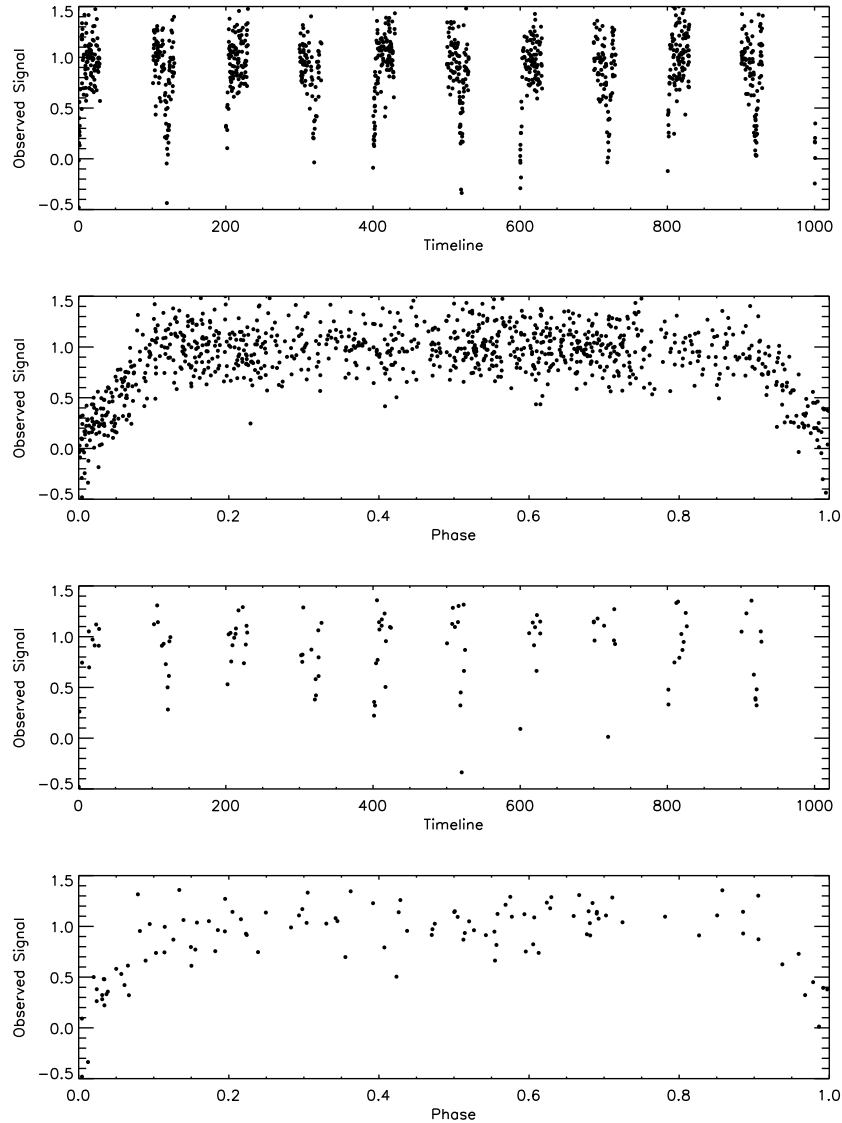


**Figure 5.** Same as for Fig. 2, but with periodic exclusion windows and with noise added, as described in § 2.3. Note how in addition to the scatter from noise, the periodicity in the sampling window produces uneven sampling in phase due to beating of the object’s period with the sampling period.

The resulting periodograms with the same timing characteristics as the previous case, are shown in Fig. 6. At this considerably large level of noise and sparse periodic sampling (panels two and four), the discriminating peaks are no

longer unique. In particular it also shows that significant levels of noise are poison to the LK algorithm, especially at sub-harmonic frequencies. But the  $\Psi$  spectrum in the final panel, which combines the information in panels two and four, still carries the correct period among the tallest peaks. This supports the notion that  $\Psi$  is a better period discriminant than either  $\Pi$  or  $\Theta$  by themselves, in the face of sparse irregular sampling with imposed periods of noisy data.

In §4, we will study the response to a real light curve with sparse sampling and multiple periodicities and gaps in sampling.

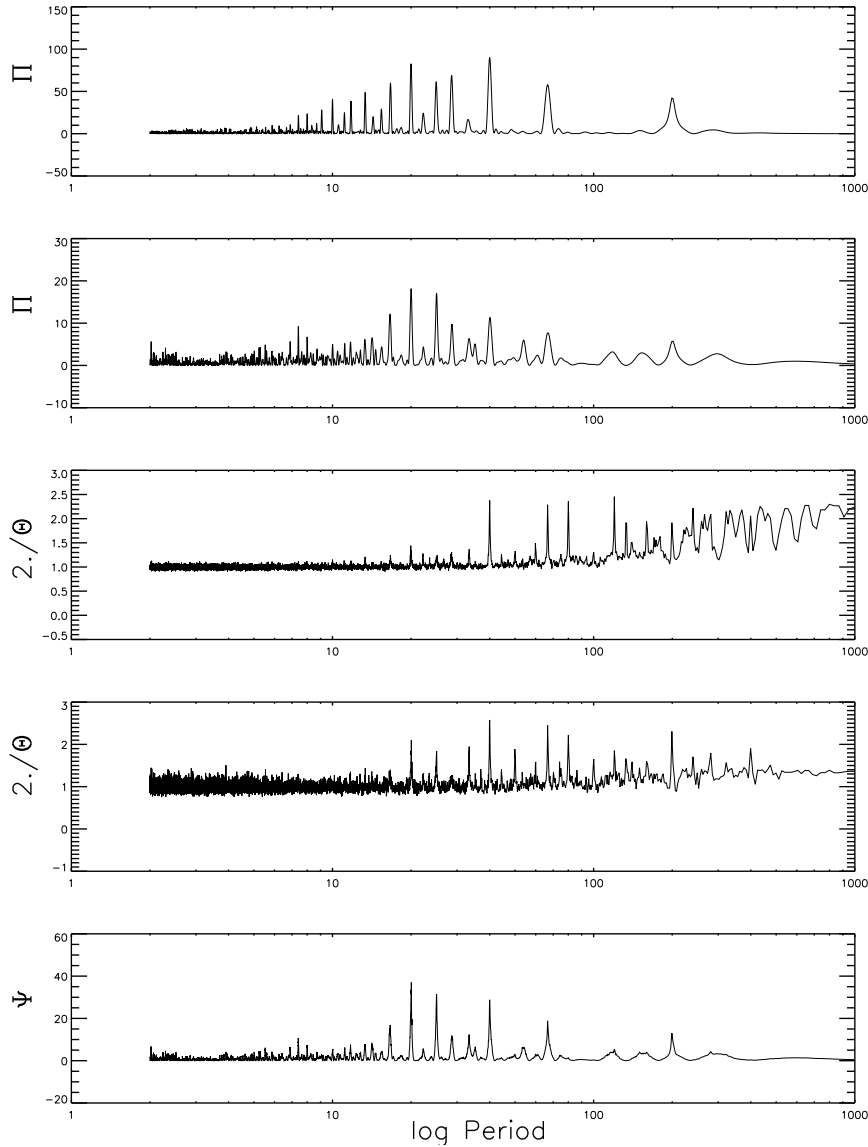


**Figure 6.** Same as for Fig. 4, but with noise added, as described in § 2.3

### 3. PRACTICAL CONSIDERATIONS

In constructing the examples in 2.3, some operational details were kept hidden to minimize distraction. However implementation of any period search algorithm involves consideration of frequency resolution, or making sure that the periodogram explores all of the structures in the power spectrum, so that peaks in periodograms are not inadvertently

skipped.

For non-regular or uneven time sampling, the usual Nyqvist criterion does not apply. We posit that the criteria for ideal resolution follow easily from a consideration of how the phases of observed points change while stepping in frequency  $f$ , as discussed by [Lafler & Kinman \(1965\)](#). If the separation in time between the first and last observations is  $T$ , then at a putative period  $P$  ( $f = 1/P$ ) the phase difference  $\phi$  between the two points is given by

$$\phi = T.f - M \quad (8)$$

where  $M$  is an integer representing the number of full cycles elapsed over the duration  $T$ . We want to take steps in  $f$  that satisfy

$$\Delta f = (\Delta\phi)_{max}/T \quad (9)$$

where  $(\Delta\phi)_{max}$  is the largest relative displacement in phase between any two points produced by a step in the sampled frequency. It is recommended that  $(\Delta\phi)_{max} \leq 1/n$  where  $n$  is the number of time-samples available, and  $1/n$  is then the mean spacing of observations in phase.

Let  $T$  be the total duration of the observations. We want to sample the power spectrum along a harmonic progression (equal intervals in  $f = 1/P$ ), for which a true Fourier series would have orthogonal coefficients. Frequencies lower than  $1/T$  are clearly undeterminable, so we begin with the low value of  $f$  as  $1/T$ . Using the result from equation 9, the  $k^{th}$  frequency  $f_k$  is thus given by :

$$f_k = 1/T + (k - 1).(\Delta\phi)_{max}/T \quad (10)$$

This progression of frequencies is then terminated at the highest desired frequency (shortest period) to be tested. The Lomb-Scargle and Lafler-Kinman algorithms are both given this frequency array over which the respective periodograms are to be evaluated.

#### 4. APPLICATION TO REAL MULTI-BAND DATA

We next derive  $\Pi$ ,  $\Theta$  and  $\Psi$  for real measurements of a real variable. The data are from a multi-band study of variable stars towards the Galactic bulge, using imaging data with the DECam instrument ([Flaugher et al. 2015](#)) on the Blanco 4m telescope at CTIO. Multi-band (DECam bands  $u, g, r, i$  and  $z$ ) multi-epoch observations of one of the variables are listed in Table 1. There are 58 well measured epochs in  $u$ , 68 in  $g$ , 69 in  $r$ , 94 in  $i$ , and 81 in  $z$ . This object, labeled B1-392 in the DECam study, was observed and reported by [Soszyński et al. \(2014\)](#) from the OGLE project as OGLE-BLG-RRLYR-11078, and shown to be an ab-type RR Lyrae star with period  $P = 0.5016240$  days. The OGLE time coverage is much more extensive than for our DECam data, and their derived period is expected to be very reliable. The DECam data include observations of a few nights in each of May, June and August of 2013, followed by parts of 3 nights in February of 2015. During the 2013 nights, up to 4 observations were made on a night, covering a span of up to 7 hours. This is thus an excellent real world example of sparse sampling infected with periodic patterns: diurnal, lunation, and a nearly 2 year gap.

Figure 7 shows various periodograms obtained from the  $g$  band data alone. The top panel shows the LS power spectrum, using  $\Delta\phi_{max} = 0.02$  and searching for periods down to  $P_{min} = 0.2$  days. It is impossible to decipher the period from this periodogram alone: it is highly confused as a result of very sparse data with impressed periodicities in the sampling and the multiple harmonics from the saw-toothed light curve of the RR Lyrae, all of which interact mutually to redistribute the power into a noise-like forest of false peaks. A peak near the period of  $\sim 0.5$  days (or  $f \sim 2$ ) exists, but is not clearly distinguishable from the many aliases. The second panel shows the LK periodogram, which is much better, but still has multiple peaks. The third panel shows the hybrid periodogram  $\Psi$  introduced in § 2.3. A prominent peak shows at  $f \approx 2$  ( $P \approx 0.5$ ) with relatively weaker features also at  $f \approx 1$  and  $f \approx 3$ , corresponding to  $P \approx 1$  and  $P \approx 0.33$  days respectively. Examination of the light curves resulting from these few putative frequencies quickly shows that the real period is close to 0.5 days. The peaks at  $f \approx 1$  and  $f \approx 3$  correspond to beat frequencies  $f_b$  of the true frequency  $f_0 \approx 2$ , in accordance with equation 7, due to the diurnal observing pattern. These are real aliases, and will express themselves through all algorithms. The fourth panel is an enlargement of the third panel, showing how the peak at  $f \approx 2$  shows fine structure: the spacing between these peaks corresponds to aliasing introduced by the  $\sim 600$  days gap in data between Aug. 2013 and Feb. 2015. Symmetry arguments (since each beat frequencies occur on both sides of the true period) and examination of the light curve folded with each of the putative periods indicated by the high peaks provides a good indication of the true period. The highest as well as most central peak of the cluster corresponds to a period  $P = 0.501628$  days, which is very close to the period reported by OGLE, and within the precision that the two year observing window permits. The lesson though, is that the  $\Psi$  periodogram provides much cleaner information than the  $\Theta$  or  $\Pi$  periodograms taken individually.

**Table 1.** Multi-epoch Multi-band photometry of B1-392

HJD-2400000.0	Mag (instrumental)	$\sigma(mag)$ (rms)	Passband
56423.6596250	22.367	0.015	r
56423.6611280	21.957	0.014	i
56423.6626230	21.914	0.016	z
56423.6641170	23.789	0.015	g
56423.6656180	27.769	0.030	u
56423.8082430	22.623	0.015	r
56423.8097370	22.164	0.014	i
56423.8112550	22.129	0.019	z
56423.8127430	24.137	0.017	g
56423.8142220	28.160	0.029	u

<sup>a</sup>All magnitudes are instrumental, but share a common zero-point within each passband

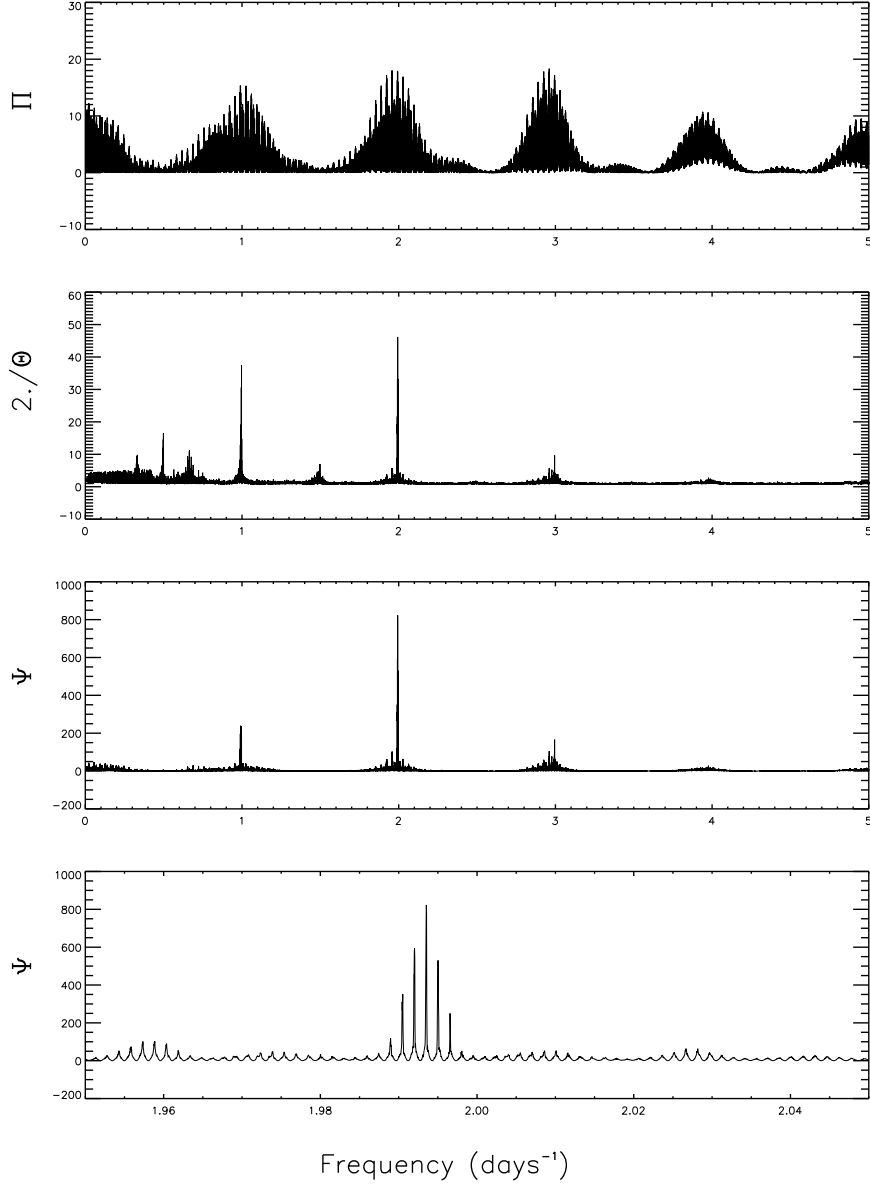
NOTE—Table 1 is published in its entirety in the electronic edition of the journal. A portion is shown here for guidance regarding its form and content.

Fig. 8 shows the  $\Psi$  periodogram in 5 passbands ( $u, g, r, i, z$ ) derived from the data on B1-392 presented in Table 1. The bottom periodogram labeled ‘ALL’, is the sum of all the periodograms from the individual passbands. In this example the object was measured sequentially in all passbands in each visit, so that they are not really asynchronous measurements. Consequently all the same aliases show up in all 5 bands. However, had the sample times been different in each of the bands, the aliases may have differed, though the peak from the true fundamental period would be common. The summed or co-averaged  $\Psi$  periodogram could then be an effective way of down-weighting specious frequencies. It could be argued that a different way of combining (e.g. taking the dot-product) the periodograms might be even more effective. However in instances where one of the bands has very little information, a more aggressive way of combining could be counterproductive. For the time-being at least, we opt for simple aggregation/co-averaging, which is the most robust against pathologies.  $\Psi_{ALL}$  peaks at a frequency corresponding to  $P = 0.501628$  days. Fig. 9 shows the light curves in each of the 5 bands when folded with this period and co-phased to a common epoch across the bands.

The  $\Psi$  periodogram in the individual bands is the product of the Lomb-Scargle power spectrum and the Laffer-Kinman statistic, neither of which retains any phase information. Thus the summed  $\Psi$  over the various bands is also expected to be independent of any phase and shape differences from band to band. To verify that this assertion is really true, we ran the B1-392 example above by injecting phase differences in the light curves in the different bands. Specifically, the observation times of all  $g$  band epochs were retarded by 0.1 days, all  $r$  band epochs by 0.2 days, all  $i$  band epochs by 0.3 days, and all  $z$  band epochs by 0.4 days. The procedure was run on this altered data set, (taking care to keep the frequency sample points identical for all passbands). The resulting summed  $\Psi_{ALL}$  spectrum was compared to that from the unaltered data: the difference was found to be *identically* zero at all sampled frequencies, demonstrating conclusively that  $\Psi$  is indeed completely agnostic of phase differences.

## 5. ESTIMATION OF SIGNIFICANCE FOR A REPORTED PUTATIVE PERIOD

Consider the true signal  $U(t)$ , as in eqn 5. If  $U$  is constant in time, and is fully sampled, the LS periodogram (or a Fourier transform) will yield a peak at zero frequency ( $f = 0$ ), and will be zero elsewhere. However, because of the missed samples, and any temporal patterns in the sampling, power in the Fourier domain will be distributed into various specious frequencies. Conversely, we can ask: how much specious power  $\rho(f)$  can be put at frequency  $f$  by a constant signal, due to gaps and patterns in the sampling? The relative power spectrum of  $W(t_i)$  ( i.e.  $S(t_i)$  with  $U(t_i)$  held constant at unity in eqn 5) provides the answer. To compare whether we have significant power  $\Pi(f)$  from a real measurement of  $S(t_i)$ , it is useful to set  $U$  to  $\alpha$ , the amplitude of  $S$ , so that  $\Pi$  and  $\rho$  are commensurate. For us to be confident that periodicity reported at frequency  $f$  is significant, we would require that  $\Pi(f) \gg \rho(f)$ .  $\rho(f)$  also has another significance. A sine or cosine true signal  $U$  with frequency  $f_0$  which is perfectly sampled will have a



**Figure 7.** The LS and LK periodograms for the  $g$  band observations in Table 1 are shown in the first and second panels respectively. The combined periodogram  $\Psi$  is shown in the third panel, with an enlargement of the structure near  $P \sim 0.5$  days in the bottom panel. See § 4 for detailed explanation.

$\delta$ -function for  $\Pi$  at  $f_0$ , which will be redistributed due to the incomplete and patterned sampling represented by  $W$  as  $\rho(f - f_0)$ . For a complex shape with many Fourier components, the power at each component  $f$  will be convolved by  $\rho$ , resulting in a complicated  $\Pi$  periodogram. Conceptually one should be able to use  $\rho$  to deconvolve  $\Pi$  (using their complex rather than absolute value forms), but in practice this is an ill-posed problem, especially in the presence of noise.

The effect of the presence of noise, and the significance of peaks in an LS periodogram is discussed in elegant detail by Horne & Baliunas (1986). Here we discuss the problem in a way that makes it easy to hybridize with the Lafler-Kinman method. Let  $\sigma(t_j)$  be the estimated rms uncertainty in the sampled value of  $S(t_j)$ . We make a random drawing from a normal distribution with this  $\sigma$ , which we denote by  $\epsilon(t_j)$ . We construct the quantity

$$S'(t_j) = \alpha \cdot W(t_j) + \epsilon(t_j) \quad (11)$$

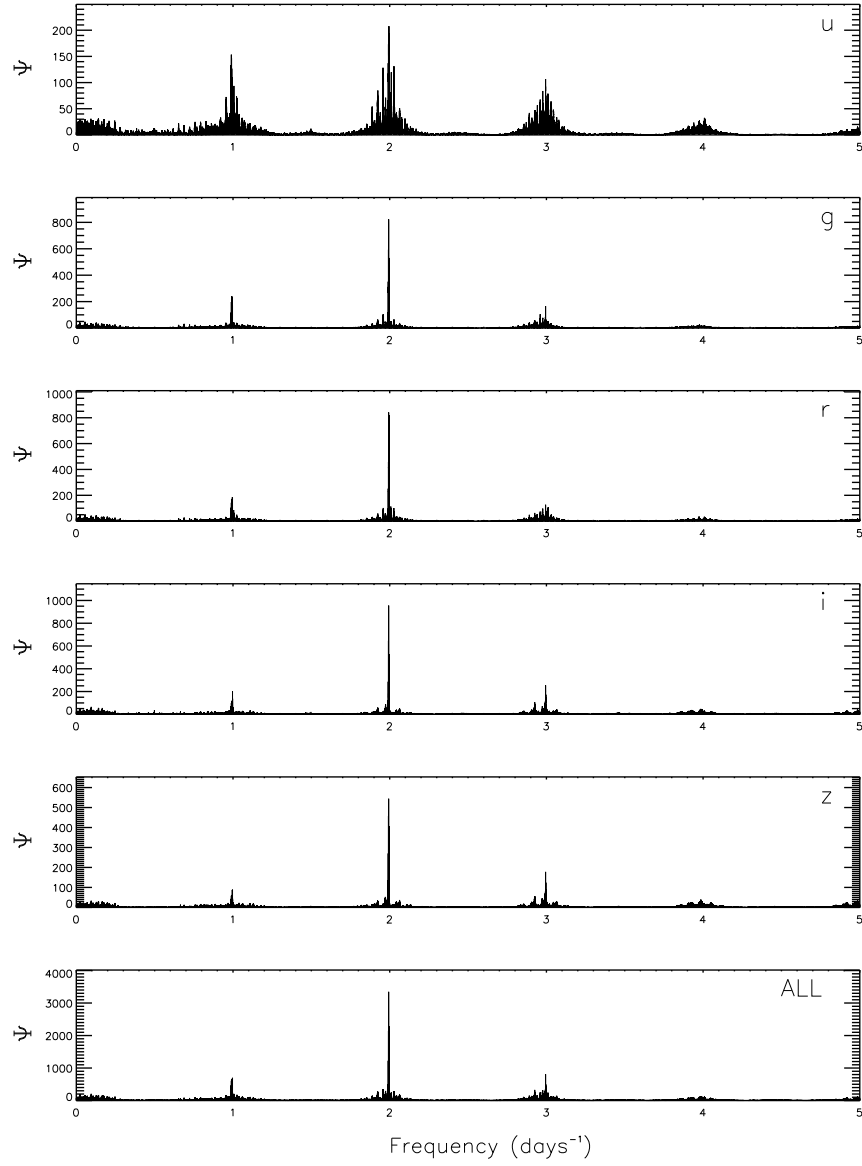


**Figure 8.** The  $\Psi$  periodogram for observations in each of the 5 bands in Table 1 are shown in the top five panels. The bottom periodogram labeled ‘ALL’ is the sum of  $\Psi$ ’s for all bands. By construction, the  $\Psi$  statistic is agnostic about any phase information, and with the power in the harmonics due to light curve shape suppressed is very weakly dependent of how the light curves change from band to band. The average  $\Psi$  is thus a useful way to aggregate information gathered at various epochs in different passbands, and so to derive the fundamental period using all of the data, as elaborated in § 4.

whose power spectrum  $\rho'(f)$  informs us whether a putative periodicity detection at  $\Pi(f)$  is significant or likely to be spurious. While  $\rho$  has been constructed above so that the total power summed over all frequencies for  $\rho$  and  $\Pi$  are the same, to assure commensurate comparison of  $\rho'$  and  $\Pi$ , it is best to rescale  $\rho'$  by a constant so that

$$\sum_f \rho'(f) = \sum_f \Pi(f) \quad (12)$$

While  $\rho$  and  $\rho'$  are well described mathematical forms for evaluating significance of a putative frequency/period from FFT analysis, the Lafler-Kinman periodogram  $\Theta$  does not appear to obey an easily characterizable mathematical

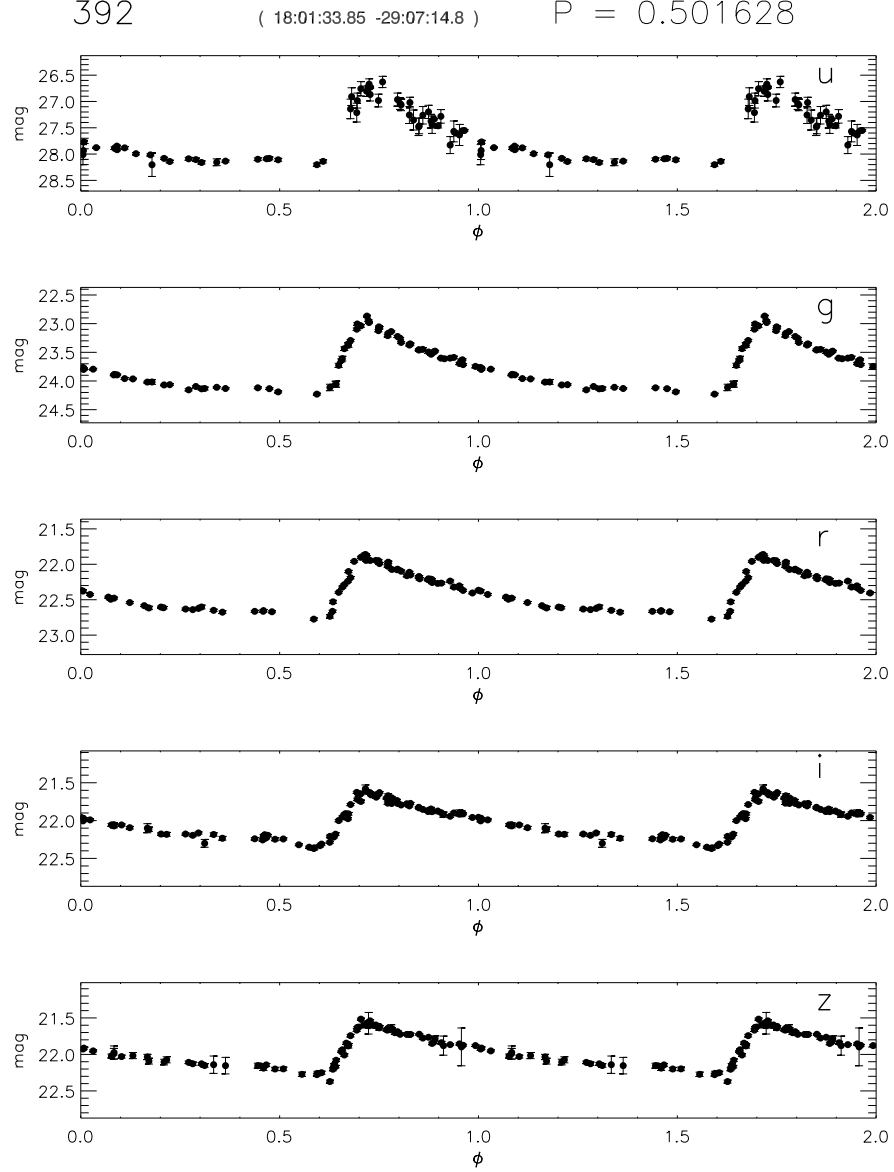


**Figure 9.** The multi-band lights curves of B1-392 at  $P = 0.501628$ , which is the frequency of the highest peak in the aggregate  $\Psi$  periodogram shown at the bottom of Fig. 8. The data are presented in Table 1.

behavior. But if we are to understand the significance of an indicated frequency/period from the hybrid function  $\Psi$ , we must account for the contribution to  $\Theta$  from the aliasing. In what follows, we attempt to simulate functions analogous to  $\rho$  and  $\rho'$  above that heed the behavior restrictions for  $\Theta$ .

Unlike the FFT case,  $\Theta$  for a noiseless steady signal is indeterminate (0/0). However, if we add the individual noise terms  $\epsilon(t_j)$ , we get deterministic values for  $\Theta$  which hover around 2.0. Any particular such periodogram depends on the particular random selection of  $\epsilon$ 's. Let us designate this periodogram by  $\eta(f)$ . The equivalent power  $\mu(f)$  in the  $\Psi$  domain from an unvarying entity in the presence of known estimates of noise (as described above), is then given by:

$$\mu(f) = \rho'(f) \cdot \eta f \quad (13)$$

$\Psi(f)$  should be greater than  $\mu(f)$  for a putative period indicated at  $f$  to be significant.

We must also consider the case of a source which varies randomly and aperiodically with an amplitude similar to that

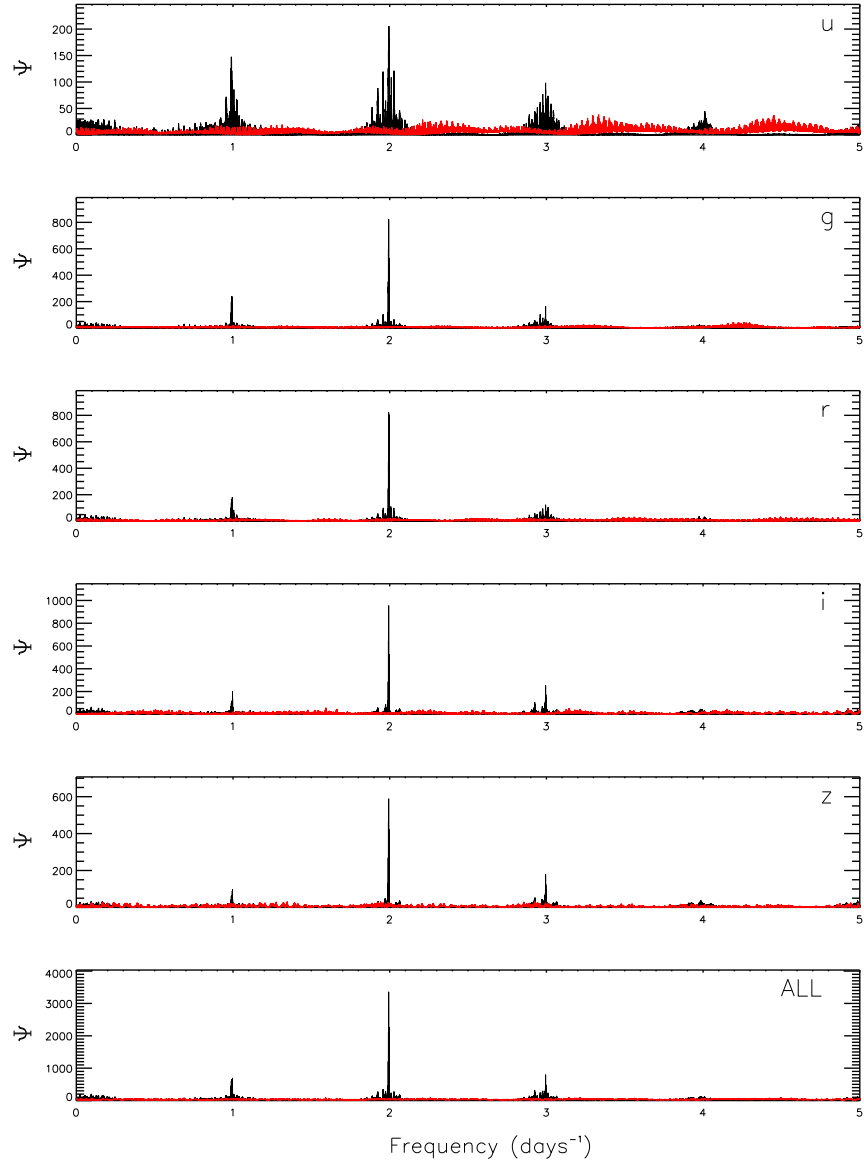


**Figure 10.** Exactly the same at Fig. 8, but with the frequency dependent threshold  $\psi_{thresh}$  for a significant ( $\sim 1\sigma$ ) periodicity detection overplotted in red. The confidence threshold calculation is discussed in § 5, which addresses both aliasing inherent in the actual sampling epochs, as well as the impact from noise from the photometry uncertainty estimates.

of the source under consideration, i.e.  $\alpha$  as used above. For this we can take the observations  $[S, t]$  and scramble them by randomly matching the observed quantity to the epoch. Let the Lomb-Scargle and Lafler-Kinman periodograms for this scrambled data-set be denoted by  $\varpi(f)$  and  $\zeta(f)$  respectively. By construction  $\varpi(f)$  should be co-normalized with  $\Pi$ , and  $\zeta(f)$  is self normalizing. For this consideration, the discriminant for  $\Psi$  is then given by:

$$\xi(f) = \varpi(f) \cdot \zeta(f) \quad (14)$$

A conservative confidence threshold  $\psi_{thresh}$  for the  $\Psi$  periodogram can be obtained by co-adding the results for the two cases above, so that

$$\psi_{thresh}(f) = \mu(f) + \xi(f) \quad (15)$$

Figure 10 shows  $\psi_{thresh}$  plotted over the  $\Psi$  periodograms for our example object B1-392.

Note that neither  $\mu(f)$  nor  $\xi(f)$  shows the aliased ‘power’ due to interaction of true periodicity with the observing window. As discussed above, this can be examined analytically for the FFT analysis by convolving  $\rho$  with the power spectrum of the source, and depends on the full power spectrum (i.e the shape of the light curve) of the source. Since for our problem, the frequency and light curve shapes are unknowns, this is not directly useful. However, it may be possible put this property of  $\rho$  to good use in an iterative fashion: once a putative period and shape are derived, it can be used to predict aliases, which are then compare to the power spectrum derived from the observations. We do not develop this any farther in this paper, and must heed the caveat that  $\psi_{thresh}$  does not account for aliases resulting from interaction of the observing windows with the periodicity in the signal: such aliases will not be identified through  $\psi_{thresh}$ .

## 6. APPLICATION TO AN LSST SIMULATION

In this final example, we consider a simulated cadence from LSST that samples the best fit template to the light curve and ephemerides of B1-392. We use the LSST Minion-1016 simulation, which is the baseline simulation (at the time of writing of this paper), and pretend that B1-392 is always imaged as part of field 1256 ( $\alpha \sim 293^\circ$  and  $\delta \sim -32^\circ$ ) which is well observed in the simulation and outside the zone of Galactic avoidance in the projected survey. This example tests the proposition that the  $\Psi$  statistics from the individual pass bands can be profitably combined even when the measurements in different bands are asynchronous. There are 900 epochs for field 1256 spread over 10 years apportioned over 6 bands, of which we use only  $u, g, r, i, z$ , for direct comparison with the example with real data in § 4. Noise drawn from a normal distribution with  $\sigma = 0.03$  mag has been added to the simulated observations of the light curve model. Fig 11 shows the individual  $\Psi$  spectra in each of the 5 bands, as well as the aggregate  $\Psi$  taken collectively. The true period at  $P = 0.501628$  days is clearly the dominant peak that appears near frequency  $f \sim 2 \text{ days}^{-1}$ . Satellite peaks at  $f \sim 1, f \sim 3, f \sim 4$  are unavoidable, given the diurnal sampling window. In the  $u$  band, where observations are restricted to within a few days of the new moon, satellite patterns due to a strong monthly window are also apparent. Clearly, with all of the data from 10 years of observations in hand, derivation of the period is straightforward, the diurnal and lunar sampling windows notwithstanding.

Fig 12 shows the results from only the first 2 years worth of observations. Note that in  $u$  and  $g$ , there are too few observations, and  $\psi_{thresh}$  dominates over  $\Psi$ . In  $r$ , and even in  $i$  there are strong false peaks. In  $z$ , which has the most observations, the true picture begins to emerge. The bottom panel, which shows the aggregate of all bands, suppresses most of the false peaks: the true signal at  $f \sim 2$  stands out, and weaker satellite peaks show up at the expected aliases. One may therefore expect that objects like B1-392 could be characterized for periodicity after 2 years of LSST observations with the regular cadence in the Minion-1016 simulation.

Since the final  $\Psi$  spectrum in this example is dominated by the  $z$ -band contribution, it is interesting to examine Fig 13, where the above case has been re-run without the  $z$ -band data. None of the individual bands indicate the correct period by themselves, but the tallest peak in the co-added  $\Psi$  periodogram corresponds to the correct value.

## 7. CONCLUDING REMARKS

The method presented here has been developed and used to examine/analyze light curves of over 20,000 putative variables from time-domain images of select fields in the Galactic bulge obtained with DECam on the 4-m Blanco telescope at CTIO. The example in §4 for the object B1-392 was one such object. This procedure was used to generate putative light curves of all of these objects, simply by identifying the maximum value in their respective multi-band co-added  $\Psi$  periodograms. Objects of interest can be selected from these ‘initial’ light-curves, and periods and light curves refined through interactive examination of any aliases present in the periodograms. Our experience has been that at least for the data at hand and the range of periods of primary interest (RR Lyrae stars), the maximum value co-added  $\Psi$  is the best estimable period in 95% of the cases. We have also compared our derived periods for  $\sim 2000$  RR Lyrae stars with those in common with OGLE. OGLE derived periods from a single passband, but had a much larger number of sample epochs, and better cadence. As for the case of B1-392, we find over 98% of the periods independently derived by the method presented here are indistinguishable from those reported by OGLE within the precision permitted by our 2-year observational baseline.

An earlier implementation of  $\Psi$  utilized a Fast Fourier Transform (FFT) instead of the Lomb-Scargle algorithm. While the former more closely adheres to the underlying assumptions of a Fourier series, it requires laying the obser-

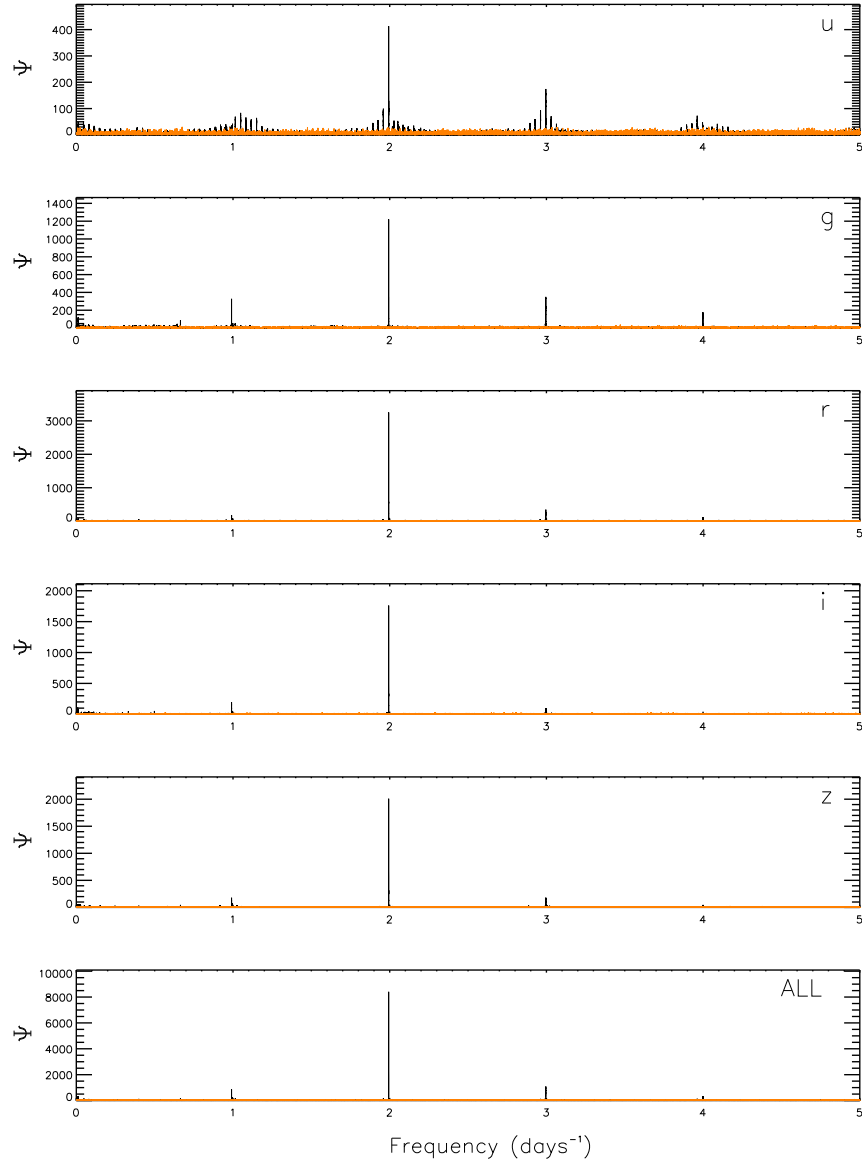


**Figure 11.** The  $\Psi$  periodograms (in black) and significance thresholds  $\psi_{thresh}$  (in orange) for an entire LSST 10 year cadence simulation in  $u, g, r, i, z$  for the light curve model for B1-392. The bottom panel shows the aggregate  $\Psi$  and  $\psi_{thresh}$  from all 5 bands.

vational timeline onto a regularly spaced temporal manifold, where time sample points with missing data are assigned zero-value, in accordance with eqn. 5. Because the FFT produces a frequency spectrum where the lowest frequency is the inverse of the total time duration, to get the frequency series that adequately samples phase intervals  $(\Delta\phi)_{max}$  (as utilized in eqn. 9), the re-sampled time sequence must be extended to a total duration  $\tau$ , where  $\tau = T/(\Delta\phi)_{max}$ . This is typically several tens of times longer than the actual observing window. Moreover, if we want to probe all periods  $P > P_{min}$ , then the re-sampled sequence must contain time steps  $<< P_{min}$ . For short values of  $P_{min}$  and large  $\tau$ , the re-sampled array becomes extremely large, and mostly full of padded zero values. While interpolation can be avoided by treating each sample point as a bin, one must take care of any situations where there are multiple observations within any time bin (by error weighted co-averaging). In practice, the construction of this artificially large re-sampled time series is inefficient. The  $\Psi$  periodograms that result from the FFT vs the LS approaches have no significant differences. While it may be of academic interest how closely the LS algorithm mimics a real Fourier

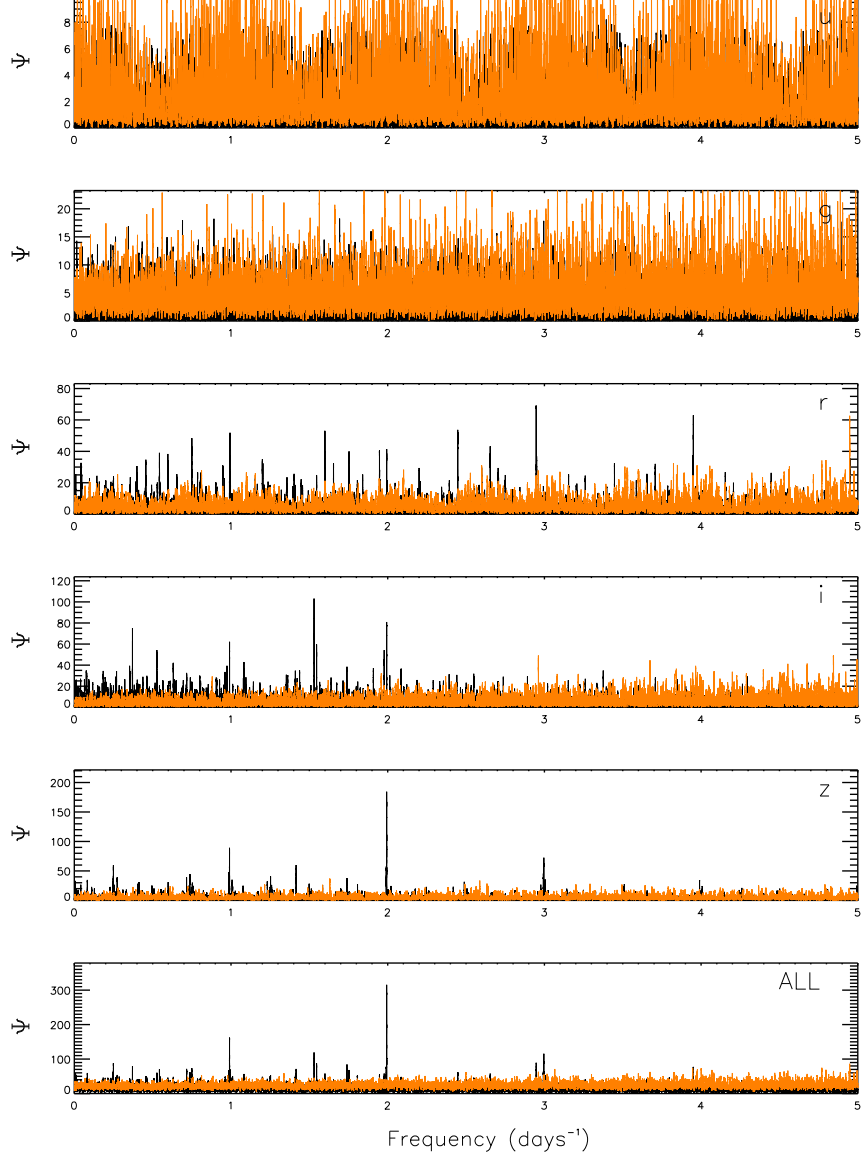


**Figure 12.** Same as Fig 11, but using only the observations in the first 2 years of the simulated survey.

series, (see [VanderPlas \(2017\)](#) for a pertinent discussion) at the end of the day the worth of a period finding procedure is in its empirical efficiency. The examples discussed also show how efficient the Lafler-Kinman algorithm really is for the cases where the light curve departs significantly from sinusoidal (albeit by visualizing it as the inverse of  $\Theta$ ).

In the example in § 4 for the observed data of B1-392, the periodograms were computed for  $\sim 173000$  frequency points ( $(\Delta\phi)_{max} = 0.02$ ). The compute time to generate the  $\Psi$  periodograms in the  $ugriz$  bands on a MacBook Pro were 2.95, 3.29, 3.27, 4.07 and 3.64 seconds respectively, totaling to 17.3 seconds for the co-added  $\Psi_{ALL}$ . The time taken scales linearly with the number of frequency points. Not much would be lost had we run with ( $(\Delta\phi)_{max} = 0.05$ ), which would cut the run times by a factor of 2.5. The implementation of this case posted on github (see Appendix) also calculates the significance thresholds  $\psi_{thresh}$ , which involves calculation of the two additional  $\Psi$  like spectra  $\mu$  and  $\xi$  (see § 5). This triples the compute time to run that example.

The multi-band periodogram method of [VanderPlas & Ivezić \(2015\)](#) has addressed the issue of combining asynchronously sampled multi-band time sequence measurements. Theirs is an extension of the Lomb-Scargle algorithm, where they seek to construct a common mode light curve that contains only low-order harmonics, and where the

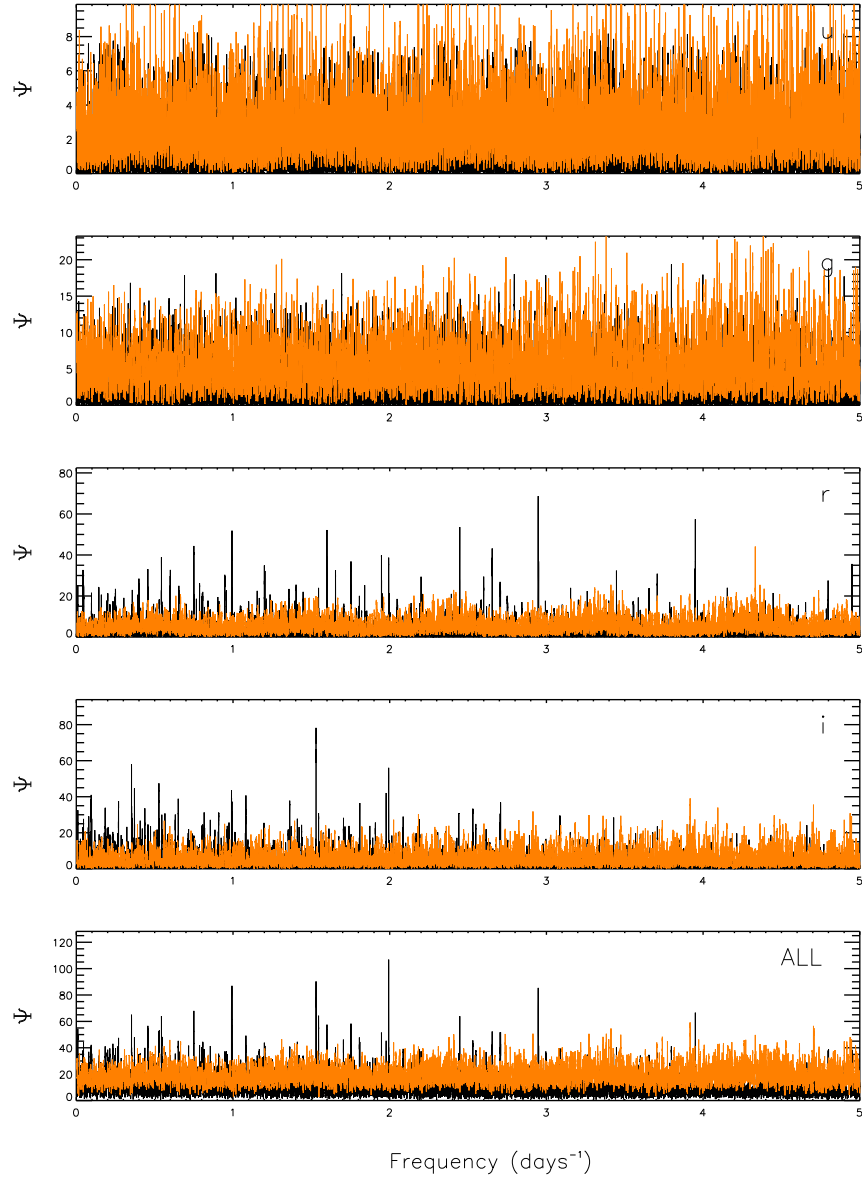


**Figure 13.** Same as Fig 12, but using only the *ugri* data. Note that while the correct period is not identifiable in any of the individual bands, in the summed  $\Psi$  periodogram it begins to emerge as the tallest peak (albeit barely).

individual channels are characterized by departures from the common mode variation. Key to their procedure is a mechanism that picks out the low-order Fourier terms that are common to all channels. Mondrik et al. (2015) prefer a multi-band extension of the analysis of variance (AoV) periodogram, which is another variant of harmonic analysis that is generalized by them for multi-band use. By contrast, in the procedure presented here the PFM based analysis is used to marginalize the higher harmonics from the harmonic analysis (and vice-versa for the sub-harmonics that appear in the PFM analysis) which effectively isolates the fundamental frequency alone that is common to all channels.

While not the objective of this paper, a performance comparison of these two methods on simulated LSST cadences for various object classes and period ranges is clearly of interest. In a very cursory effort we have also run our procedure on a posted example<sup>2</sup> of the VanderPlas & Ivezić (2015) algorithm, which uses the multi-band light curve of RR Lyrae #1013184 in SDSS Stripe 82 (Sesar et al. 2010). The run times to produce the  $\Psi$  periodograms for this example

<sup>2</sup> We modified the Jupyter notebook example in <http://nbviewer.jupyter.org/github/astroML/gatspy/blob/master/examples/MultiBand.ipynb> to run locally in our machine and have local access to the data

with 67000 frequency sample points were about 1.2 seconds in each of the 5 passbands, totaling 6 seconds to obtain  $\Psi_{ALL}$ . Our run with the *gatspy* [VanderPlas & Ivezić \(2015\)](#) code on this example, with a similar number of sampled frequencies ran in a little under 3 seconds. While there are many details to sort out to make a like-to-like comparison, it appears that they both run on comparable time-scales.

This work has its roots in conversations with Gautham Narayan, who has been engaged in employing period finding methods on existing survey data in the context of building algorithms for the transient event broker ANTARES ([Saha et al. 2016](#)). We thank the referee for perceptive and useful comments.

*Software:* Psearch ([Saha 2017](#))

## APPENDIX

### A. CODE FOR PROCESSES AND ALGORITHMS IN THE IDL LANGUAGE

The algorithms discussed in this paper are coded in the IDL language, and are available through *github* at <https://github.com/AbhijitSaha/Psearch> and Zenodo ([Saha 2017](#)). The data for the RR Lyrae stars B1-392, as well as for the LSST year simulation used in this paper are also available from that location. Descriptions and instructions for use are given in comments within the routines, and/or in the accompanying *README* file. Also included is the *scargle.pro* routine from the NASA IDL astronomy library. Two examples of how to use the code are also provided, which works with a) the B1-392 data-set that is provided, and b) the simulation of B1-392 as it might be observed by LSST as it is discussed in this paper.

## REFERENCES

- Alcock, C., Axelrod, T. S., Bennett, D. P., et al. 1992, in Astronomical Society of the Pacific Conference Series, Vol. 34, Robotic Telescopes in the 1990s, ed. A. V. Filippenko, 193–202
- Alcock, C., Allsman, R. A., Axelrod, T. S., et al. 1996, ApJ, 461, 84
- Chambers, K. C., Magnier, E. A., Metcalfe, N., et al. 2016, ArXiv e-prints, arXiv:1612.05560
- Drake, A. J., Djorgovski, S. G., Mahabal, A., et al. 2009, ApJ, 696, 870
- Flaugher, B., Diehl, H. T., Honscheid, K., et al. 2015, AJ, 150, 150
- Graham, M. J., Drake, A. J., Djorgovski, S. G., et al. 2013, MNRAS, 434, 3423
- Horne, J. H., & Baliunas, S. L. 1986, ApJ, 302, 757
- Koch, D. G., Borucki, W. J., Basri, G., et al. 2010, ApJL, 713, L79
- Lafler, J., & Kinman, T. D. 1965, ApJS, 11, 216
- Law, N. M., Kulkarni, S. R., Dekany, R. G., et al. 2009, PASP, 121, 1395
- Lomb, N. R. 1976, Ap&SS, 39, 447
- Mondrik, N., Long, J. P., & Marshall, J. L. 2015, ApJL, 811, L34
- Pojmanski, G. 2002, Acta Astron., 52, 397
- Rau, A., Kulkarni, S. R., Law, N. M., et al. 2009, PASP, 121, 1334
- Saha, A. 2017, Psearch, v.1.0, Zenodo, doi:10.5281/zenodo.917040
- Saha, A., Wang, Z., Matheson, T., et al. 2016, in Proc. SPIE, Vol. 9910, Society of Photo-Optical Instrumentation Engineers (SPIE) Conference Series, 99100F
- Scargle, J. D. 1982, ApJ, 263, 835
- Sesar, B., Ivezić, Ž., Grammer, S. H., et al. 2010, ApJ, 708, 717
- Soszyński, I., Udalski, A., Szymański, M. K., et al. 2014, Acta Astron., 64, 177
- Stellingwerf, R. F. 1978, ApJ, 224, 953
- Udalski, A., Szymański, M., Kaluzny, J., Kubiak, M., & Mateo, M. 1993, Acta Astron., 43, 69
- VanderPlas, J. T. 2017, ArXiv e-prints, arXiv:1703.09824
- VanderPlas, J. T., & Ivezić, Ž. 2015, ApJ, 812, 18